



Superb impact resistance of nano-precipitation-strengthened high-entropy alloys



Ao Fu^a, Bin Liu^{a,*}, Zezhou Li^b, Tao Yang^c, YuanKui Cao^a, Junyang He^a, Bingfeng Wang^a, Jia Li^d, Qihong Fang^d, Xingwang Cheng^b, Marc A. Meyers^e, Yong Liu^a

^a State Key Laboratory of Powder Metallurgy, Central South University, Changsha 410083, China

^b School of Materials Science and Engineering, Beijing Institute of Technology, Beijing 100081, China

^c Department of Mechanical Engineering, City University of Hong Kong, 999077, the Hong Kong Special Administrative Region of China

^d State Key Lab of Advanced Design and Manufacturing for Vehicle Body, Hunan University, Changsha 410082, China

^e Department of Mechanical and Aerospace Engineering, University of California San Diego, La Jolla, CA 92093, USA

ARTICLE INFO

Keywords:

High-entropy alloy
Dynamic response
Adiabatic shear band
Deformation mechanism
Molecular dynamics simulation

ABSTRACT

Critical engineering applications, such as landing gears and armor protection, require structural materials withstanding high strength and significant plastic deformation. Nanoprecipitate-strengthened high-entropy alloys (HEAs) are considered as promising candidates for structural applications due to their enhanced strength and exceptional work-hardening capability. Herein, we report a FeCoNiAlTi-type HEA that achieves ultrahigh gigapascal yield strength from quasi-static to dynamic loading conditions and superb resistance to adiabatic shear failure. This is accomplished by introducing high-density coherent L1₂ nanoprecipitates. Multiscale characterization and molecular dynamics simulation demonstrate that the L1₂ nanoprecipitates exhibit multiple functions during impact, not only as the dislocation barrier and the dislocation transmission medium, but also as energy-absorbing islands that disperse the stress spikes through order-to-disorder transition, which result in extraordinary impact resistance. These findings shed light on the development of novel impact-resistant metallic materials.

1. Introduction

Dynamic response of structural materials is crucial to engineering applications, such as aerospace, defense technologies, and high-speed trains [1–3]. With the growing demands for high strain-rate service conditions, structural materials need to retain high strength and toughness at high strain rates. The family of high-entropy alloys (HEAs) with a single face-centered cubic (FCC) crystal structure and transitional elements exhibits remarkable damage tolerance at high strain rates due to the extremely high strain-rate hardening ability resulting from multiple strengthening mechanisms (e.g., forest dislocations, mechanical twinning, phase transitions, etc. [4–16]). For example, the FeCoCrNiMn HEA presents outstanding fracture toughness over a wide temperature range, and the formation of adiabatic shear bands (ASBs) is retarded up to a very large shear strain ~ 7 [17]. The Fe₄₀Mn₂₀Cr₂₀Ni₂₀ HEA shows high strength of 1412 MPa and high tensile ductility of 33.3% at the high strain rate [18]. The CoCrNi HEA exhibits excellent impact shear toughness at both room and low temperatures [12]. However, such

single-phase FCC-type HEAs generally show a relatively low impact strength, which seriously limits their practical applications.

Recent studies have revealed that the introduction of coherent nanoprecipitates can be an effective strategy toward superior strength-ductility synergy. The dual-phase nanostructured HEAs are expected to push the strength-ductility envelope into the previously inaccessible territory [19–25]. Among them, the typical L1₂-strengthened Co-Cr-Ni-Al-Ti HEA [19], Fe-Co-Ni-Al-Ti HEA [21], and Fe-Co-Cr-Ni-Al-Ti HEA [22] have been proven to exhibit a superior combination of strength and ductility. Their excellent tensile properties can be attributed to the dense nanoscale precipitates and dynamically activated plastic deformation mechanisms, particularly a strong effect of microbanding, twinning, and phase transition. Although the quasi-static deformation mechanisms of nanoprecipitate-strengthened HEAs have been extensively elucidated, there is a dearth of studies on the dynamic response, deformation mechanisms, and failure behavior. Nanoprecipitates can not only improve the quasi-static mechanical properties of the materials, but also possess an obvious strengthening effect on the

* Corresponding author.

E-mail address: binliu@csu.edu.cn (B. Liu).

Peer review under the responsibility of Central South University.

<https://doi.org/10.1016/j.apmate.2025.100277>

Received 20 December 2024; Received in revised form 20 January 2025; Accepted 27 January 2025

Available online 7 February 2025

2772-834X/© 2025 Central South University. Publishing services by Elsevier B.V. on behalf of KeAi Communications Co. Ltd. This is an open access article under the CC BY-NC-ND license (<http://creativecommons.org/licenses/by-nc-nd/4.0/>).

dynamic properties [26–29]. For instance, nickel-based superalloys possess a high strength in the high-speed deformation because the high density of γ' nanoprecipitates can effectively hinder dislocation motion, thereby greatly enhancing the strain-hardening capability [26]. Meanwhile, dislocation cutting through the nanoprecipitates will promote the formation of anti-phase boundaries, which can further increase the strain hardening rate and contribute to the high strength [30]. Moreover, the nanoprecipitates can be regarded as the “unit” for energy absorption. The fine dispersion of high-density nanoprecipitates can absorb more energy [27–29], increasing damage resistance. However, there is still little information concerning the dynamic behavior of these nanoprecipitate-strengthened HEAs under very high strain rates exceeding 10^3 s^{-1} .

Inspired by the above ideas, we employed the precipitation-strengthening strategy to prepare a dual-phase $(\text{FeCoNi})_{84}\text{Al}_7\text{Ti}_7$ HEA (denoted here as 7AlTi) with a high-volume fraction of coherent and ordered L_{12} nanoprecipitates by powder metallurgy. We found that this alloy exhibits superior strength and damage resistance than other traditional alloys at very high strain rates due to the incorporation of the ductile L_{12} nanoprecipitates. At high strain rates, additional deformation mechanisms (such as phase transformation) that are extremely difficult to occur in quasi-static condition [21], are activated in the 7AlTi HEA, contributing to the significant improvement of dynamic properties. In particular, it is important to note that these coherent nanoprecipitates can not only act as dislocation barriers during high-speed impact, but also serve as energy-absorbing islands, enabling the alloy to exhibit high strength without damage, which is the main reason for its excellent impact resistance.

2. Results and discussion

2.1. Microstructure

The 7AlTi HEA was prepared by hot extrusion of gas-atomized powders (Fig. S1). Its crystal structure was examined by X-ray diffraction (XRD) (Fig. 1a and S2), revealing that it is mainly composed of FCC and L_{12} phases. In addition, there is a small fraction of submicron-sized L_{21} phase (Figs. S3 and S4), mainly distributed at the grain boundaries. The electron backscatter diffraction-inverse pole figure (EBSD-IPF) map in

Fig. 1b shows that the microstructure is composed of typical recrystallized equiaxed grains with an average size of $\sim 20 \mu\text{m}$. The electron channeling contrast imaging (ECCI) image in Fig. 1b further shows that the high-density near-spherical L_{12} particles (average diameter of $\sim 39.5 \text{ nm}$, Figs. S5 and 1c) are uniformly distributed in the matrix, with a volume fraction as high as $\sim 58\%$. The details of the duplex microstructure were analyzed by transmission electron microscopy (TEM) and high-resolution TEM (HR-TEM). The selected area electron diffraction (SAED) and fast Fourier transformation (FFT) patterns (Fig. 1d) show that the L_{12} nanoprecipitates are perfectly coherent with the FCC matrix with a very small lattice mismatch around 0.17% from the XRD characterization (Fig. S2). The chemical composition of the nanoprecipitates was investigated by TEM Energy Dispersive Spectroscopy (EDS) elemental mapping, and these nanoparticles are rich in Ni, Ti, and Al, but rare in Co and Ni (Fig. S6).

2.2. Dynamic compression behavior

The mechanical response of the 7AlTi HEA under quasi-static and dynamic uniaxial compression is presented in Fig. 2a. At room temperature, the yield strength at 0.001 s^{-1} can reach 1090 MPa, nearly 6 times that of the single-phase FeCoNi base alloy (Fig. S7a). More remarkably, the 7AlTi HEA exhibits better strain-hardening capability than the FeCoNi alloy after yielding (Fig. S7b). This can be attributed to the hardening effect from the high-density L_{12} -type nanoprecipitates [30, 31]. At the very high strain rate of 2400 s^{-1} , its yield strength increases to 1350 MPa indicating a positive correlation between the strength and strain rate (Fig. S8a). The strain rate sensitivity (SRS), m , can be used to reveal the variations of the flow stresses with respect to the logarithmic strain rates [32]. The SRS of the 7AlTi HEA can be divided into two separate regions, i.e., quasi-static SRS (m_s) and dynamic SRS (m_d). It can be seen that the dynamic SRS is much higher than the quasi-static value, mainly because the deformation-rate-controlling mechanisms change from thermally activated dislocation motion to the drag of phonons and electrons on dislocation motion [16]. Fig. S8a compares the dynamic SRS of the 7AlTi HEA with many other HEAs and traditional high-performance materials, including FeCoCrNiMn HEA, Inconel 718, etc. [4,16,33–42]. Evidently, the 7AlTi HEA ($m_d=0.38$) shows superior dynamic SRS. It was reported that the existence of chemical short-range

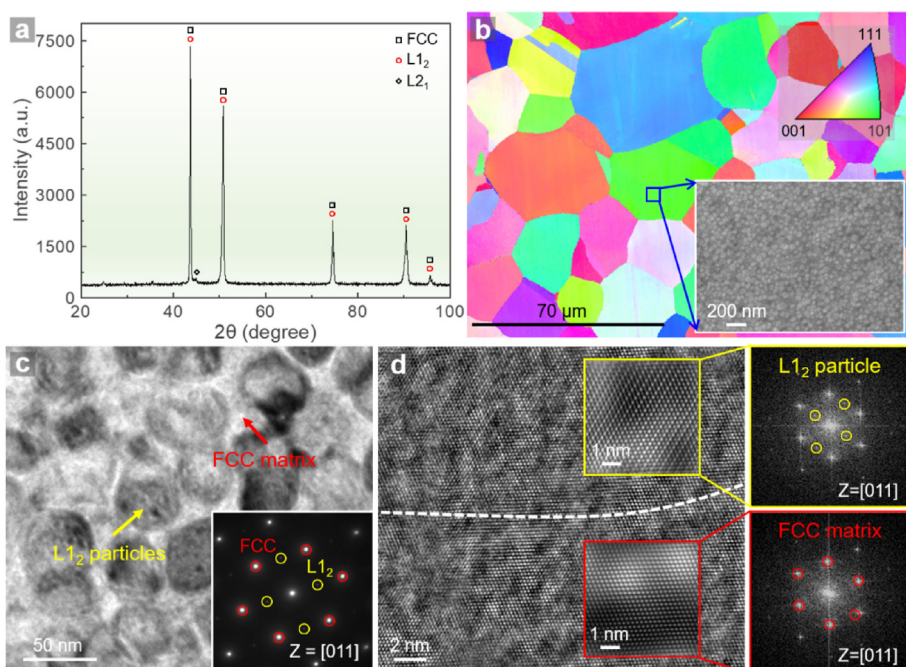


Fig. 1. Initial microstructure of the 7AlTi HEA. (a) XRD pattern showing the crystal structures; (b) EBSD-IPF map and SEM image showing the typical equiaxed grains; (c) TEM image showing the highly dispersed L_{12} nanoprecipitates within the FCC matrix. The inset showing the corresponding SAED pattern; (d) HR-TEM image showing the interfacial coherency between the L_{12} nanoprecipitates and FCC matrix. The FFT image highlighted by the red rectangle confirms the FCC matrix in the zone axis of [011]. By contrast, the superlattice spots shown in the yellow rectangle region's FFT image revealing the L_{12} -structured nanoprecipitates.

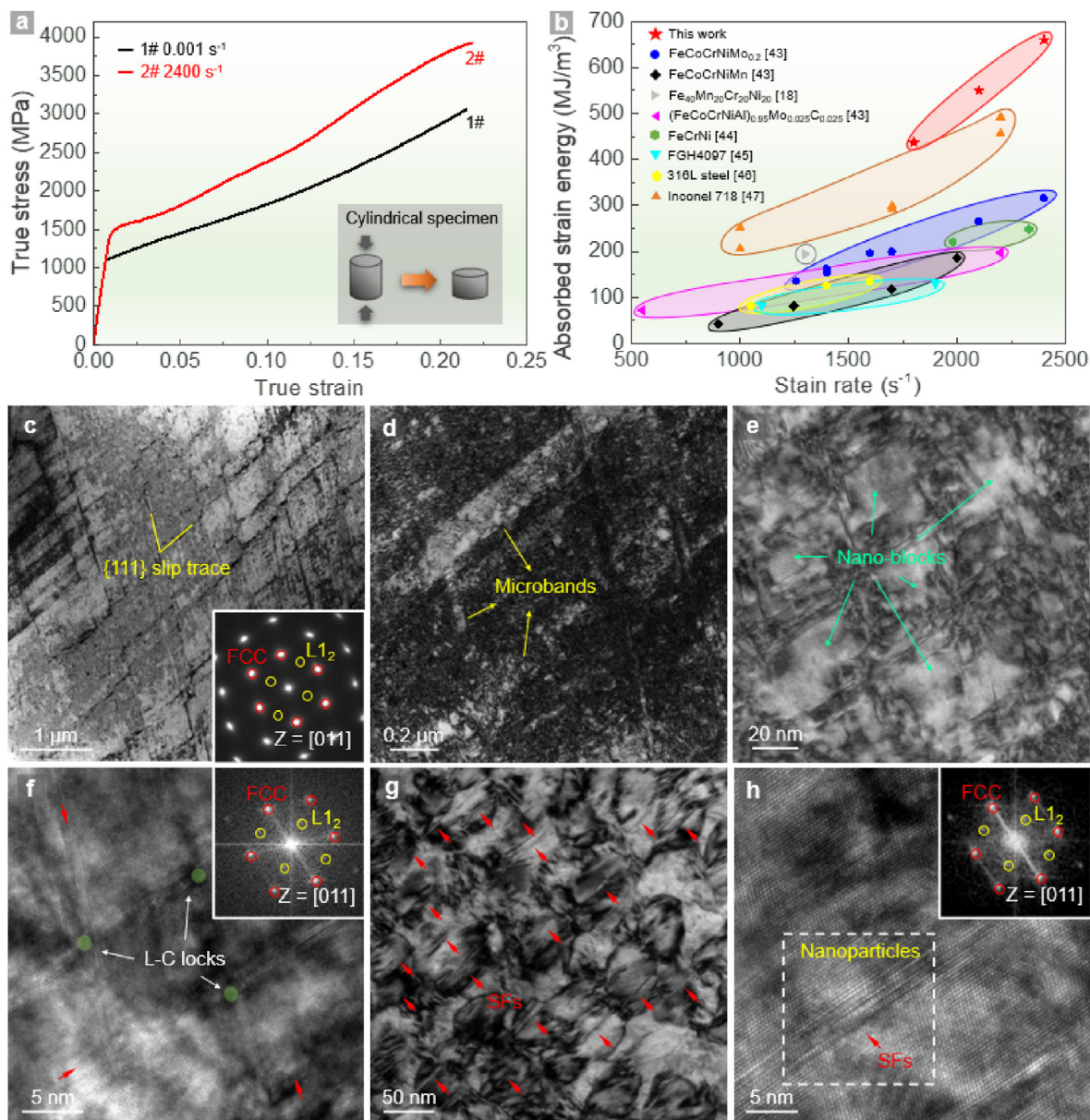


Fig. 2. Dynamic compression behavior of the 7AlTi HEA subjected to dynamic impact with a loading strain rate of 2400 s^{-1} . (a) Stress-strain curves under quasi-static compression ($\dot{\epsilon}_d=10^{-3}\text{ s}^{-1}$) and dynamic compression ($\dot{\epsilon}_d=2400\text{ s}^{-1}$); (b) Absorbed strain energy of the 7AlTi HEA under dynamic loading compared with other high-performance materials [18,43–47]. The absorbed strain energy is calculated by integrating the area under the true stress-strain curves [29,43]. (c–f) Bright-field (BF) TEM images showing the (c) dislocation planar slip along the {111} primary slip planes, (d) deformation-induced microbands, (e) nano-blocks induced by the crossed SFs, and (f) L-C locks; (g) BF TEM and (h) HRTEM images showing the L1₂ nanoprecipitates are sheared by SFs, and the insert FFT pattern in (h) confirms the ordered structure of the nanoprecipitates in the FCC matrix.

order/clusters (SROs/SRCs) as well as the larger Peierls-Nabarro (PN) barrier can increase the SRS of FCC-type HEAs [4,16]. In this HEA, the large number of fine nanoprecipitates can act as short-distance obstacles playing a decisive role in limiting the dislocation movement, which further contributes to the improvement of the SRS [28]. In addition, as shown in Fig. 2b, we further compare the absorbed strain energy of various high-performance materials, including 7AlTi HEA, FeCoCrNiMn HEA, FeCoCrNiMo_{0.2} HEA, FeCrNi HEA, Inconel 718, and 316 steel, etc. [21,43–47], under dynamic loading ($>500\text{ s}^{-1}$). Prominently, the absorbed strain energy of the 7AlTi HEA at 2400 s^{-1} can reach 660 MJ/m^3 , much higher than that of other high-performance materials. Therefore, the 7AlTi HEA exhibits ultrahigh gigapascal yield strength from the quasi-static to dynamic loading regime, resulting in resistance to damage.

To understand the high strain-rate deformation mechanisms, the microstructures after dynamic compression were characterized. As shown in Fig. 2c–2h, the density of deformation substructure is higher than that of the sample after quasi-static deformation (Fig. S9). Massive dislocation arrays are activated on the {111} slip planes, forming high-density dislocation networks throughout the grains and accommodating deformation (Fig. 2c). The deformation-induced twinning and martensitic transformation that often occur in the single-phase FCC HEAs with low stacking-fault energy (SFE) are absent in the 7AlTi HEA. This is mainly because the FeCoNi matrix has a high SFE, and the presence of high-density nanoprecipitates is suggested to increase the nucleation barrier for mechanical twinning or phase transformation [21]. However, deformation-induced microbands are very prevalent in the 7AlTi HEA (Fig. 2d), and act as the dominant deformation mechanism under

dynamic compression.

Additionally, the interaction of high-density deformation-induced SFs leads to extensive formation of Lomer-Cottrell (L-C) locks in the FCC matrix and $L1_2$ nanoprecipitates, which further evolve into diamond-shaped nano-blocks (Fig. 2e-2f). This kind of unique substructure promotes dislocation accumulation and refine the grain size when plastic strains increase, resulting in a prominent “dynamic Hall-Petch” effect [31]. The geometric phase analysis (GPA) in Fig. S10 also quantifies the noticeable strain fields in the nano-blocks, and the strain field mainly resides along the L-C locks, implying that stronger forces are necessitated for the nano-blocks on passing dislocations. As a result, various grain refinement mechanisms can be activated in the 7AlTi HEA, such as SFs, L-C locks, slip bands, and microbands, effectively enhancing the hardening ability through the “dynamic Hall-Petch” effect. The beneficial effect was also observed in other FCC materials [48–50], for example, manganese steels. In addition, the dispersed $L1_2$ nanoprecipitates (Fig. S11) have an important influence on the deformation behavior of the 7AlTi HEA. The HRTEM images in Fig. 2g-h shows that the $L1_2$ nanoprecipitates can be sheared by SFs. During the deformation process, the coherent $L1_2$ nanoprecipitates effectively hinder the dislocation movement and thereby greatly increase the yield strength through the dislocation shearing mechanism. The strengthening contribution of the $L1_2$ nanoprecipitates was estimated to be ~ 795 MPa, as shown in Supplementary Materials [20,24,25,50–54]. At the same time, they can relieve stress concentration by cooperating with the deformation of the matrix, which contributes to the high plasticity [55,56].

2.3. Dynamic shear behavior

Because of the excellent strain/strain-rate hardening effects and decent resistance against thermal softening of the 7AlTi HEA

(Figs. S7–S8) [17,57–61], it is difficult for adiabatic shear localization to initiate in the uniformly deformed cylindrical samples. The formation of ASBs is usually recognized as an important failure mechanism in extremely high strain-rate loading [17]. In order to investigate the possible adiabatic shear localization behavior, a special geometry of hat-shaped samples (Fig. S12a) was used to induce forced shear into a narrow region and create large shear strains [62]. Fig. 3a shows the shear stress vs. strain relationship of a hat-shaped sample with a displacement of 1.14 mm. It can be found that the strain rate of the hat-shaped sample ($9.6 \times 10^5 \text{ s}^{-1}$) is significantly higher than that of the cylindrical samples. Meanwhile, a distinct ASB is formed only at a large imposed shear strain of ~ 4.6 . It can be seen from Fig. S12c that the width of the ASB is $\sim 2 \mu\text{m}$, which is much narrower than that of the imposed shear region ($\sim 100 \mu\text{m}$). These results indicate that the ASB is difficult to form in the 7AlTi HEA. Materials with higher hardenability and thermal softening resistance show superior shear localization resistance [11]. The 7AlTi HEA has exceptionally excellent hardenability (strain hardening and strain-rate hardening) and decent thermal softening resistance, meaning that the ASB hardly appears under the high strain-rate loading, which is crucial for engineering applications. The plots for the impact shear toughness and shear yield strength for the 7AlTi HEA along with other high-performance materials [12,17,43,63–70], such as FeCoCrNi HEA, CoCrNi HEA, 316L steel, and Ti-6Al-4V, etc., are presented in Fig. 3b. As indicated, the 7AlTi HEA exhibits a superior combination of impact shear toughness and shear yield strength when compared with other high-performance materials, offering larger safety margin against impact failure.

The microstructure in the highly deformed shear region was characterized to reveal the deformation mechanisms. Due to the extremely high shear strain rate and shear strain, the microstructure inside the imposed shear region is completely different from the deformation substructure

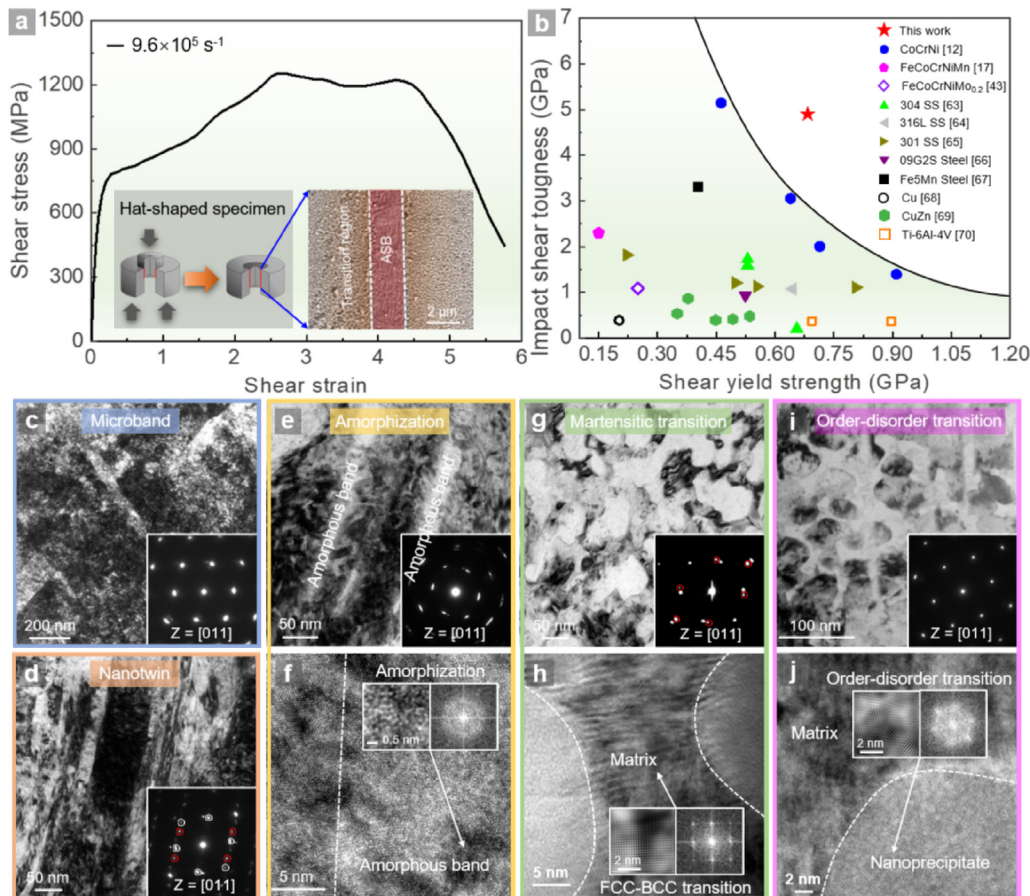


Fig. 3. Dynamic shear behavior of the 7AlTi HEA subjected to dynamic impact with a loading strain rate of $9.6 \times 10^5 \text{ s}^{-1}$. (a) Shear stress vs. shear strain for the hat shaped specimen; (b) Impact shear toughness as a function of the shear yield strength for the 7AlTi HEA, along with the data for other high-performance materials [12,17,43,63–70]. The impact shear toughness can be calculated by integrating the area under the shear stress-strain curve [12]. TEM image showing the deformation microstructure inside the transition regions: (c) microbands, (d) nanotwins, (e–f) amorphous bands, (g–h) martensitic transition, and (i–j) order-to-disorder transition.

after quasi-static or dynamic uniaxial compression. The shear region mainly consists of the inner ASB and the outer transition region. The grains in the ASB are completely refined and are ultrafine equiaxed (Fig. S12d). These ultrafine grains are formed by significant rotational dynamic recrystallization, which has been described in many metallic materials [17]. Since the ASB is formed by the local shear instability, here we focus on the microstructural evolution in the transition region.

The deformation substructure within the transition region mainly involves high-density microbands (Fig. 3c), twins (Fig. 3d), martensites (Fig. 3g-h), and amorphous bands (Fig. 3e-3f). The deformation-induced twins and amorphous bands are usually difficult to appear in the L_{12} nanoprecipitate-strengthened Fe-Co-Ni-Al-Ti HEAs [71], which implies that high strain-rate and large strain promote the emergence of these deformation mechanism. The multiple deformation behavior can continuously refine the grains during shear deformation, which enhance the strain hardening rate, retarding shear localization to higher shear strain levels. The TEM images in Fig. 3g-h shows the appearance of large-area body-centered cubic (BCC) martensite. The activation of martensitic transition can be explained through the following argument. Firstly, the matrix of the L_{12} nanoprecipitate-strengthened Fe-Co-Ni-Al-Ti HEA, such as the Al8Ti6 [71], contains a higher Co content and a lower Ni content, showing a significant martensitic phase transition tendency. Al-containing HEA systems are also favorable for the FCC-BCC martensitic transition [72], and the chemical compositions of the matrix in the 7AlTi HEA are listed in Table S1. Secondly, the large shear strain in the transition region greatly promotes the martensitic transition [72,73].

In addition, we observed a very interesting phenomenon: the L_{12} nanoprecipitates undergo an order-to-disorder transition accompanied by an amorphization under such an extremely high strain rate, as shown in Fig. 3i-3j. However, this amorphization did not lead to the change in the chemical composition of the L_{12} nanoprecipitates (Fig. S13). This indicates that L_{12} nanoprecipitates are the main carriers of deformation in the nanoprecipitate-strengthened materials, and shows a strong

disordering tendency under the severe shear of dislocation pairs. This order-to-disorder transition is actually another additional deformation mechanism in the L_{12} nanoprecipitate-strengthened HEAs besides deformation-induced microbanding, twinning, martensitic transition, and amorphization, contributing to the improvement of strain-hardening capability [74].

To gain further insights into deformation mechanisms under extreme impact loading, the deformation processes in the 7AlTi HEA are investigated by atomic simulations (see Supplementary Materials). Fig. 4a shows the atomic snapshots of the 7AlTi HEA at different times under the high-speed shock wave. It can be seen that multiple deformation pathways, including high-density dislocations, microbands, twins, BCC martensite, and amorphous segments, can be activated. However, the amorphous regions appear at high deformation strain due to the sufficiently high system energy required for driving the amorphization, which is quite different from the twin and stacking fault mechanisms in the precipitate-free 7AlTi HEA. The 3D planar defect network (Fig. 4b) shows the details of deformation microstructure, and the amorphous segments are nucleated mainly at the intersection of multiple SFs where the local stresses are more concentrated. To understand the deformation mechanisms associated with the L_{12} nanoprecipitates, the local microstructure evolution near the precipitate is investigated in detail from cross-sectional slices (Fig. 4c). From the snapshots in the high-magnification view (Fig. 4d), it can be seen that the L_{12} nanoprecipitates can act as dislocation barriers and dislocation transmission media during the deformation process, thereby greatly improving the strain-hardening capability. High-density planar defects lead to significant dislocation and SF accumulation after passing through the L_{12} nanoprecipitates. This in turn generates a large local stress field. Since the order-to-disorder transition requires a large amount of energy for nucleation, the transition preferentially occurs at defect interaction sites inside the L_{12} nanoprecipitates, where the defect density is high and the local stress is large. In addition, the deformation microstructure of the nanoprecipitate-

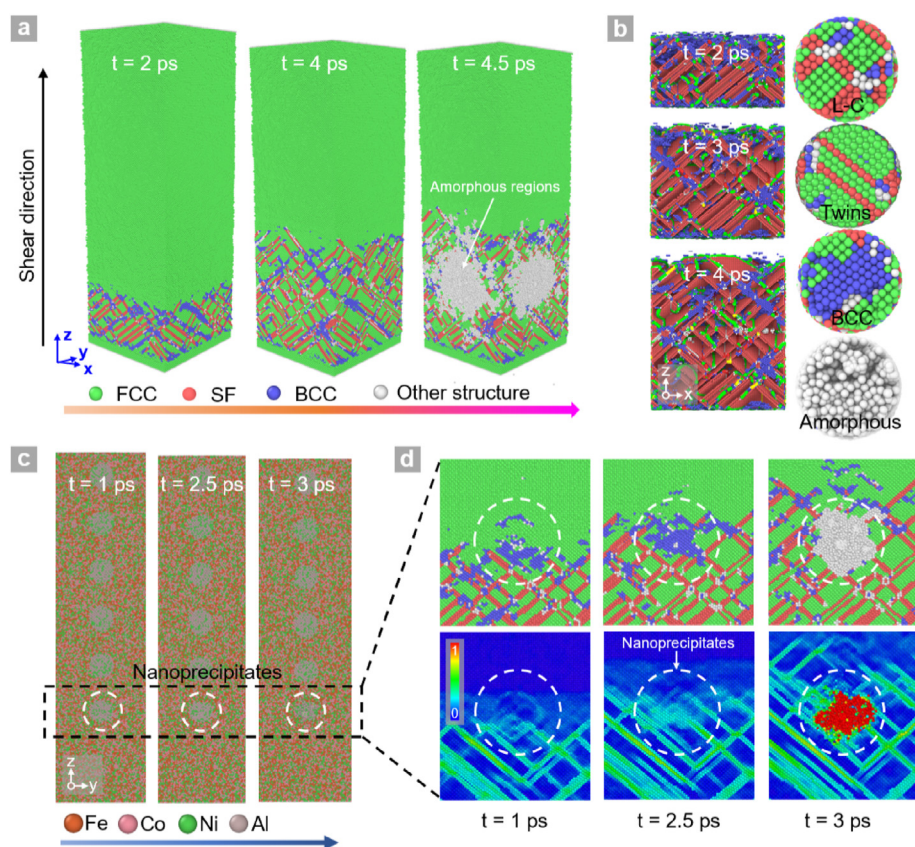


Fig. 4. Predicted deformation microstructure of the 7AlTi HEA subjected to dynamic impact from atomic simulations. (a) Full view of the deformation microstructure at different impact moments (2, 4, and 4.5 ps). The green, red, blue, and gray atoms represent FCC structure, SF structure, BCC structure, and disordered structure, respectively. (b) 3D planar defect network, including SFs, microbands, L-C locks, twins, BCC segments, and amorphous regions. (c) Disorder transition of L_{12} nanoprecipitates during the impact process. The atoms are colored according to atomic type, and the L_{12} nanoprecipitates are marked by white circles. (d) Shear strain fields around the L_{12} nanoprecipitates. High shear strains induced by the interaction of planar defects lead to the order-to-disorder transition of the L_{12} nanoprecipitates.

free 7AlTi HEA is also investigated under the same impact condition (Fig. S14). It can be clearly seen that the density of the deformation microstructures is significantly lower, and the amorphous phase is difficult to nucleate. Therefore, the introduction of the L_{12} nanoprecipitates can activate multiple deformation pathways in the 7AlTi HEA, especially amorphization, which contributes to the improvement of strength and toughness. At the same time, the high-density L_{12} nanoprecipitates can dissipate more impact energy through order-to-disorder transition, thereby enhancing the damage resistance.

2.4. Illustration of deformation mechanism

Based on the above analysis, we schematically summarize the strain-rate-dependent deformation mechanism of the 7AlTi HEA in Fig. 5. Under quasi-static loading, the dislocations, SFs, and microbands are the main deformation substructure. As the strain rate increases, the dominant deformation mechanism remains unchanged, but the density of the deformation substructure increases significantly. Meanwhile, more planar slip systems are activated, which greatly promotes the formation of a large number of L-C locks and interaction between SFs and L_{12} nanoprecipitates, resulting in a sustained hardening ability and excellent dynamic mechanical properties. At the extremely high strain rate, deformation-induced twinning, martensitic transition, and amorphization which are difficult to form in the L_{12} nanoprecipitate-strengthened HEAs appear. These additional deformation mechanisms work together with dislocation slip, L-C locks, and microbands to provide multiple pathways for the dissipation of the impact strain energy, preventing the generation and further development of ASBs. It is particularly noteworthy that, unlike single-phase FCC HEA, the high-density L_{12} nanoprecipitates exhibit multifunctionality during deformation, which can not only hinder dislocation motion, improving the strength through the particle shear mechanism, but also serve as dispersed energy-absorbing sinks under extremely high impact loading, greatly consuming the impact strain energy through the order-to-disorder transition. Thus, the material is endowed with excellent dynamic mechanical properties.

3. Conclusions

In summary, we found that by introducing a high density of coherent L_{12} nanoprecipitates, the single-phase FCC HEA system attains superior dynamic properties to most structural materials. The coherent nanoprecipitates can effectively improve the strength through particle

shearing mechanism. At large shear strains under dynamic deformation, these nanoparticles can also provide an additional deformation mechanism for the 7AlTi HEA in addition to dislocation slipping, twinning, microbanding, and martensitic transition. The order-to-disorder transition in nanoparticles coordinates plastic deformation and dissipates impact strain energy. These multiple deformation pathways endow the 7AlTi HEA with excellent dynamic properties, making it a viable candidate for extreme load applications. We believe that this alloy design strategy of introducing coherent nanoprecipitates into high-performance materials can greatly improve the development of impact-resistant structural materials.

4. Materials and methods

4.1. Materials preparation

The 7AlTi HEA was fabricated by the powder metallurgy method. Firstly, high-purity (>99.99%) Fe, Co, Ni, Al, and Ti raw materials were melted into liquid melt, and then atomized by Ar with 4 MPa atomization pressure. The received powders were shown in Figs. S1a and S1b. Subsequently, the powders with a mean particle size (d_{50}) of $\sim 28 \mu\text{m}$ (Fig. S1c) were encapsulated into a 45# steel tank ($\phi 50 \times 150 \text{ mm}$), preheated at $1150 \text{ }^\circ\text{C}$ for 1 h, and immediately hot extruded to a bar with an extrusion ratio of 7:1, followed by air cooling to the room temperature. The chemical compositions of the gas-atomized powders and extruded samples were listed in Table S2. In addition, the FeCoNi base alloy was prepared by arc melting for comparison. All the samples were repeatedly melted for at least 5 times to promote the chemical homogeneity, and then dropped cast into a $15 \text{ mm} \times 15 \text{ mm} \times 50 \text{ mm}$ copper mold.

4.2. Quasi-static and dynamic mechanical testing

Quasi-static compression experiments were conducted on an Instron universal testing machine. Dynamic compression and shear experiments were performed by a split Hopkinson pressure bar (SHPB) system. Cylindrical samples ($\phi 4 \times 6 \text{ mm}$) were used in the quasi-static/dynamic compression testing. Hat-shaped samples were used in the dynamic shear experiments, and a series of hood heights ($h=0.42, 0.6, 1.14, 1.58 \text{ mm}$) were designed to generate ASBs (Fig. S15). The incident and transmission signals were collected by the dynamic strain indicator to calculate the true stress, true strain, and strain rate. The details of the calculation process can be found in previous work [13,14]. All the

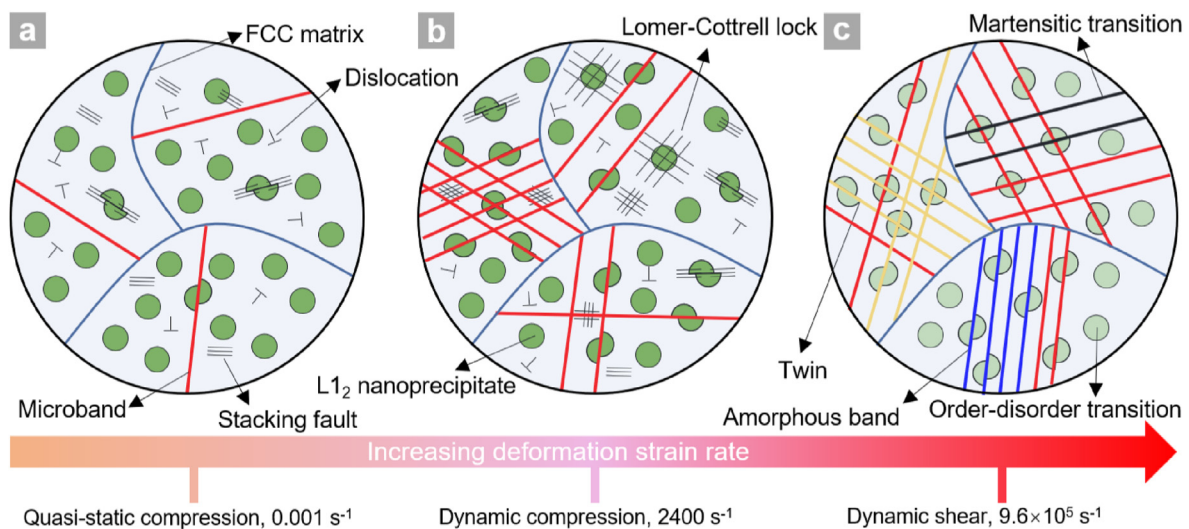


Fig. 5. Schematic illustration of the deformation mechanisms in the 7AlTi HEA during plastic straining. (a) Dislocations, SFs and microbands; (b) Dislocations, SFs, L-C locks and microbands; (c) Microbands, nanotwins, amorphous bands, martensitic transition, and order-to-disorder transition.

samples were cut along the extrusion direction by electro-discharge machining and then mechanically polished with SiC papers.

4.3. Microstructural characterization

Concentrations were measured by inductively coupled plasma atomic emission spectrometer (ICP-AES, ICAP-7600) and oxygen/nitrogen analyzer (TCH-600). Phase constitutions were analyzed by an X-ray diffractometer (XRD, Advance D8) with Cu K α radiation in a scanning angle range from 20° to 100°. The lattice mismatch value between the L1₂ nanoprecipitates and FCC matrix was calculated by a Rietveld refinement analysis (MAUD software) of the XRD data (Fig. S3). The lattice mismatch (δ) can be estimated by the following equation: $\delta = 2(\alpha_{\text{nanoprecipitate}} - \alpha_{\text{matrix}}) / (\alpha_{\text{nanoprecipitate}} + \alpha_{\text{matrix}})$ [23], where $\alpha_{\text{nanoprecipitate}}$ is the lattice parameter for the L1₂ nanoprecipitates and α_{matrix} is the lattice parameter for the FCC matrix. Specific heat capacity was measured by a differential scanning calorimeter (DSC, Netzsch STA 449 F3) at a heating/cooling rate of 10 K/min. Microstructure was analyzed by a scanning electron microscope (SEM, Helios Nanolab G3 UC) equipped with an electron backscatter diffraction (EBSD) instrument. Chemical analyses at the macroscale were performed on an Electron Probe Micro-analyzer (EPMA, JXA-8530F). SEM/EPMA specimens were mechanically polished, and EBSD specimens were electro-polished in a solution of 10% HClO₄ and 90% C₂H₅OH at -30 °C with a voltage of 30 V. The detailed microstructure was investigated using a transmission scanning electron microscope (TEM, Tecnai G2 F20) coupled with energy dispersive spectrometer (EDS). The volume fraction of different phases was measured from their area fractions by a commercial software package (Image-J). At least one hundred particles were included to obtain the average value. Conventional TEM specimens were prepared by mechanically grinding and followed by electro-polishing to a thickness of electron transparency. Site-specific focused ion beam (FIB) TEM specimens in the shear region were prepared by a Thermo Fisher Scientific HELIOS FEI FIB machine with a 25 kV–30 kV Ga ion beam.

4.4. MD simulation

Molecular dynamics (MD) simulations were performed by the large-scale atomic/molecular massively parallel simulator (LAMMPS) [75]. The FeCoNiAl HEA was modeled by the classical embedded atom method (EAM) potential [76]. To investigate the shock loading, a single-crystal HEA containing a coherent nanoprecipitate with a 5 nm radius was constructed and oriented along the crystallographic axes of x-[100], y-[010] and z-[001]. The Fe, Ni, Co and Al atoms in the FeCoNiAl HEA were randomly distributed, while the nanoprecipitates were composed solely of Ni and Al. The FeCoNiAl HEA model was created by starting with only Fe atoms, followed by randomly substituting the Fe atoms with Co, Ni, and Al atoms. The nanoprecipitates are assumed to only contain Ni and Al. The shock-loaded sample dimensions were 17.9×17.9×55.0 nm³, comprising 1,550,000 atoms. The constructed structures were first equilibrated by the conjugate gradient (CG) method to minimize energy and subsequently annealed at 5 K and 0 bar pressure in the NPT ensemble (Nose-Hoover thermostat and Parrinello-Rahman barostat [77,78]) for 100 ps. During the thermal relaxation, the pressure was controlled by the Parrinello-Rahman method, while the temperature regulation was achieved via the Nose-Hoover technique with a damping constant of 100 MD steps. A time step of 1 fs was chosen to ensure accurate equilibration, with periodic boundary conditions applied in all directions. The low temperature of 5 K was specifically selected to mitigate potential artifacts arising from high strain rates. Shock loading was applied along the z-axis by introducing a rigid piston at the base of the sample, moving at a constant velocity of 1.1 Å/ps (1.1 km/s). Periodic boundary conditions were imposed in the lateral directions (x and y), while the z-direction remained free. The piston-induced planar shock wave generated a strain rate of 0.021–0.022/ps over a 15 ps duration. Atomistic interactions involving the piston and the sample were modeled using the same

interatomic potential, though the piston atoms were excluded from the MD simulations. The NVE ensemble was employed during shock loading, with atomic trajectories integrated using a predictor-corrector method and a time step of 1 fs. Crystallographic structures, dislocation lines, and atomic trajectories were visualized using OVITO [79]. The common neighbor analysis (CNA) [80] identified local atomic structures. Dislocation evolution was analyzed via the dislocation extraction algorithm.

CRedit authorship contribution statement

Ao Fu: Writing – original draft, Methodology, Investigation, Formal analysis. **Bin Liu:** Supervision, Project administration, Funding acquisition. **Ze Zhou Li:** Methodology, Investigation. **Tao Yang:** Methodology, Conceptualization. **Yuan Kui Cao:** Formal analysis, Data curation. **Junyang He:** Investigation. **Bingfeng Wang:** Investigation, Formal analysis. **Jia Li:** Data curation, Conceptualization. **Qihong Fang:** Writing – review & editing, Resources. **Xingwang Cheng:** Resources, Conceptualization. **Marc A. Meyers:** Methodology, Investigation. **Yong Liu:** Supervision, Conceptualization.

Data and materials availability

All data needed to evaluate the conclusions in the paper are present in the paper and/or the Supplementary Materials.

Declaration of competing interest

The authors declare that they have no known competing financial interests or personal relationships that could have appeared to influence the work reported in this paper.

Acknowledgements

We would like to deeply appreciate the National Natural Science Foundation of China (Grant No. 52020105013 and 52401223), Natural Science Foundation of Hunan Province (Grant No. 2022JJ20001) and Science and Technology Foundation Strengthening Program (Grant No. 6142902210104). T.Y. is grateful for the financial support from the Research Grants Council of the Hong Kong Special Administrative Region, China (Grant No. C1020-21G).

Appendix A. Supplementary data

Supplementary data to this article can be found online at <https://doi.org/10.1016/j.apmate.2025.100277>.

References

- [1] Z. Li, S. Zhao, R.O. Ritchie, M.A. Meyers, Mechanical properties of high-entropy alloys with emphasis on face-centered cubic alloys, *Prog. Mater. Sci.* 102 (2019) 296–345.
- [2] J.C. Williams, E.A. Starke, Progress in structural materials for aerospace systems, *Acta Mater.* 51 (2003) 5775–5799.
- [3] Y. Tang, D.Y. Li, Dynamic response of high-entropy alloys to ballistic impact, *Sci. Adv.* 8 (2022) eabp9096.
- [4] T.W. Zhang, S.G. Ma, D. Zhao, Y.C. Wu, Y. Zhang, Z.H. Wang, J.W. Qiao, Simultaneous enhancement of strength and ductility in a NiCoCrFe high-entropy alloy upon dynamic tension: micromechanism and constitutive modeling, *Int. J. Plast.* 124 (2020) 226–246.
- [5] D.B. Miracle, O.N. Senkov, A critical review of high entropy alloys and related concepts, *Acta Mater.* 122 (2017) 448–511.
- [6] W. Li, D. Xie, D. Li, Y. Zhang, Y. Gao, P.K. Liaw, Mechanical behavior of high-entropy alloys, *Prog. Mater. Sci.* 118 (2021) 100777.
- [7] D. Xu, M. Wang, T. Li, X. Wei, Y. Lu, A critical review of the mechanical properties of CoCrNi-based medium-entropy alloys, *Microstructures* 2 (2022) 2022001.
- [8] Y.J. Yang, Y. Dong, S.C. Liu, S.G. Duan, C.Q. Li, P. Zhang, A novel AlCo_{1.2}Cr_{0.8}FeNi_{2.1} eutectic high entropy alloy with excellent corrosion resistance, *J. Alloys Compd.* 998 (2024) 175006.
- [9] Y. Wu, P.K. Liaw, R. Li, W. Zhang, G. Geng, X. Yan, G. Liu, Y. Zhang, Relationship between the unique microstructures and behaviors of high-entropy alloys, *Int. J. Min. Met. Mater.* 31 (2024) 1350–1363.

- [10] J. Man, B. Wu, G. Duan, L. Zhang, X. Du, Y. Liu, C. Esling, Super-high strength of a CoCrNiFe based high entropy alloy, *J. Mater. Sci. Technol.* 177 (2024) 79–84.
- [11] S. Zhao, Z. Li, C. Zhu, W. Yang, Z. Zhang, D.E. Armstrong, P.S. Grant, R.O. Ritchie, M.A. Meyers, Amorphization in extreme deformation of the CrMnFeCoNi high-entropy alloy, *Sci. Adv.* 7 (2021) eabb3108.
- [12] Y. Ma, F.P. Yuan, M.X. Yang, P. Jiang, E. Ma, X.L. Wu, Dynamic shear deformation of a CrCoNi medium-entropy alloy with heterogeneous grain structures, *Acta Mater.* 148 (2018) 407–418.
- [13] Y. Tang, R. Wang, B. Xiao, Z. Zhang, S. Li, J. Qiao, S. Bai, Y. Zhang, P.K. Liaw, A review on the dynamic-mechanical behaviors of high-entropy alloys, *Prog. Mater. Sci.* 135 (2023) 101090.
- [14] R. Liu, C. Wang, B. Liu, Y. Liu, P.K. Liaw, B. Wang, Microstructure and formation mechanisms of nanotwins in the shear band in a FeCoNiCrMo_{0.2} high-entropy alloy, *J. Mater. Res. Technol.* 20 (2022) 2719–2733.
- [15] Z. Zhang, Y. Ma, S. Qin, J. Wang, M. Yang, P. Jiang, X. Wu, F. Yuan, Unusual phase transformation and novel hardening mechanisms upon impact loading in a medium entropy alloy with dual heterogeneous structure, *Intermetallics* 151 (2022) 107747.
- [16] X.L. Liu, Y.D. Wu, Y.S. Wang, J.B. Chen, R. Bai, L. Gao, Z. Xu, W.Y. Wang, C.W. Tan, X.D. Hui, Enhanced dynamic deformability and strengthening effect via twinning and microbanding in high density NiCoFeCrMoW high-entropy alloys, *J. Mater. Sci. Technol.* 127 (2022) 164–176.
- [17] Z. Li, S. Zhao, S.M. Alotaibi, Y. Liu, B. Wang, M.A. Meyers, Adiabatic shear localization in the CrMnFeCoNi high-entropy alloy, *Acta Mater.* 151 (2018) 424–431.
- [18] Y.Z. Wang, Z.M. Jiao, G.B. Bian, H.J. Yang, H.W. He, Z.H. Wang, P.K. Liaw, J.W. Qiao, Dynamic tension and constitutive model in Fe₄₀Mn₂₀Cr₂₀Ni₂₀ high-entropy alloys with a heterogeneous structure, *Mater. Sci. Eng. A* 839 (2022) 142837.
- [19] N. Yao, T. Lu, K. Feng, B. Sun, R. Wang, J. Wang, Y. Xie, P. Zhao, B. Han, X. Zhang, S. Tu, Ultrastrong and ductile additively manufactured precipitation-hardening medium-entropy alloy at ambient and cryogenic temperatures, *Acta Mater.* 236 (2022) 118142.
- [20] L. Han, Z. Rao, I.R. Souza Filho, F. Maccari, Y. Wei, G. Wu, A. Ahmadian, X. Zhou, O. Gutfleisch, D. Ponge, D. Raabe, Z. Li, Ultrastrong and ductile soft magnetic high-entropy alloys via coherent ordered nanoprecipitates, *Adv. Mater.* 33 (2021) 2102139.
- [21] T. Yang, Y.L. Zhao, Y. Tong, Z.B. Jiao, J. Wei, J.X. Cai, X.D. Han, D. Chen, A. Hu, J.J. Kai, K. Lu, Y. Liu, C.T. Liu, Multicomponent intermetallic nanoparticles and superb mechanical behaviors of complex alloys, *Science* 362 (2018) 933–937.
- [22] J.Y. He, H. Wang, H.L. Huang, X.D. Xu, M.W. Chen, Y. Wu, X.J. Liu, T.G. Nieh, K. An, Z.P. Lu, A precipitation-hardened high-entropy alloy with outstanding tensile properties, *Acta Mater.* 102 (2016) 187–196.
- [23] Y.L. Zhao, T. Yang, Y.R. Li, L. Fan, B. Han, Z.B. Jiao, D. Chen, C.T. Liu, J.J. Kai, Superior high-temperature properties and deformation-induced planar faults in a novel L1₂-strengthened high-entropy alloy, *Acta Mater.* 188 (2020) 517–527.
- [24] Z. Liu, X. Zhao, Y. Wu, Q. Chen, B. Yang, P. Wang, Z. Chen, C. Yang, Superior high-temperature properties and deformation-induced planar faults in a novel L1₂-strengthened high-entropy alloy, *Rare Met.* 41 (2022) 2853–2863.
- [25] Z.Y. Jia, S.Z. Zhang, J.T. Huo, C.J. Zhang, L.W. Zheng, F.T. Kong, H. Li, Heterogeneous precipitation strengthened non-equiatom NiCoFeAlTi medium entropy alloy with excellent mechanical properties, *Mater. Sci. Eng. A* 834 (2022) 142617.
- [26] K.B. Yuan, W.G. Guo, D.W. Li, P.H. Li, Y. Zhang, P.C. Wang, Influence of heat treatments on plastic flow of laser deposited Inconel 718: testing and microstructural based constitutive modeling, *Int. J. Plast.* 136 (2021) 102865.
- [27] L. Ye, G. Gu, X. Zhang, D. Sun, H. Jiang, P. Zhang, Dynamic properties evaluation of 2519A aluminum alloy processed by interrupted aging, *Mater. Sci. Eng. A* 590 (2014) 97–100.
- [28] B.Z. Long, Y. Zhang, C.H. Guo, Y. Cui, L.X. Sun, D. Chen, F.C. Jiang, T. Zhao, G. Zhao, Z.W. Zhang, Enhanced dynamic mechanical properties and resistance to the formation of adiabatic shear band by Cu-rich nano-precipitates in high-strength steels, *Int. J. Plast.* 138 (2021) 102924.
- [29] Z. Gao, X. Zhang, M.A. Chen, Influence of strain rate on the precipitate microstructure in impacted aluminum alloy, *Scripta Mater.* 59 (2008) 983–986.
- [30] B. Gwalani, S. Gangireddy, Y. Zheng, V. Soni, R.S. Mishra, R. Banerjee, Influence of ordered L1₂ precipitation on strain-rate dependent mechanical behavior in a eutectic high entropy alloy, *Sci. Rep.* 9 (2019) 6371.
- [31] N. Li, J. He, Y. Zhou, J. Gu, S. Ni, M. Song, Strain rate effects on the mechanical responses in Mo-alloyed CoCrNi medium entropy alloys, *Mater. Sci. Eng. A* 856 (2022) 143944.
- [32] S. Liu, M. Hu, L. Xiao, G. Feng, K. Song, W. Song, J. Qiao, Effects of strain rate and low temperature on dynamic behaviors of additively manufactured CoCrFeMnNi high-entropy alloys, *Mater. Sci. Eng. A* 913 (2024) 147100.
- [33] W. Lee, C. Lin, T. Chen, H. Chen, Dynamic mechanical behaviour and dislocation substructure evolution of Inconel 718 over wide temperature range, *Mater. Sci. Eng. A* 528 (2011) 6279.
- [34] J.M. Park, J. Moon, J.W. Bae, M.J. Jang, J. Park, S. Lee, H.S. Kim, Strain rate effects of dynamic compressive deformation on mechanical properties and microstructure of CoCrFeMnNi high-entropy alloy, *Mater. Sci. Eng. A* 719 (2018) 155–163.
- [35] W.S. Lee, C.F. Lin, C.Y. Liu, F.T. Tzeng, Impact properties of 304L stainless steel GTAW joints evaluated by high strain rate of compression tests, *J. Nucl. Mater.* 335 (2004) 335–344.
- [36] W.S. Lee, C.Y. Liu, T.N. Sun, Deformation behavior of Inconel 690 super alloy evaluated by impact test, *J. Mater. Process. Technol.* 153 (2004) 219–225.
- [37] Z. Li, B. Wang, S. Zhao, R.Z. Valiev, K.S. Vecchio, M.A. Meyers, Dynamic deformation and failure of ultrafine-grained titanium, *Acta Mater.* 125 (2017) 210–218.
- [38] X. Zhong, Q. Zhang, M. Ma, J. Xie, M. Wu, S. Ren, Y. Yan, Dynamic compressive properties and microstructural evolution of Al_{1.19}Co₂CrFeNi_{1.81} eutectic high entropy alloy at room and cryogenic temperatures, *Mater. Des.* 219 (2022) 110724.
- [39] X. Zhong, Q. Zhang, J. Xie, M. Wu, F. Jiang, Y. Yan, Z. Wang, Mechanical properties and microstructure of the Al_{0.3}CoCrFeNiTi_{0.3} high entropy alloy under dynamic compression, *Mater. Sci. Eng. A* 812 (2021) 141147.
- [40] N. Kumar, Q. Ying, X. Nie, R.S. Mishra, Z. Tang, P.K. Liaw, R.E. Brennan, K.J. Doherty, K.C. Cho, High strain-rate compressive deformation behavior of the Al_{0.1}CrFeCoNi high entropy alloy, *Mater. Des.* 86 (2015) 598–602.
- [41] K. Jiang, J.G. Li, B. Gan, T. Ye, L.Y. Chen, T. Suo, Dynamically compressive behaviors and plastic mechanisms of a CrCoNi medium entropy alloy at various temperatures, *Acta Mech. Sin.* 38 (2022) 421550.
- [42] L. Wang, J. Qiao, S. Ma, Z. Jiao, T. Zhang, G. Chen, D. Zhao, Y. Zhang, Z. Wang, Mechanical response and deformation behavior of Al_{0.6}CoCrFeNi high-entropy alloys upon dynamic loading, *Mater. Sci. Eng. A* 727 (2018) 208–213.
- [43] W. Li, Y. Huang, Z. Xie, H. Chen, W. Li, B. Liu, B. Wang, Mechanical property and cellular structure of an additive manufactured FeCoNiCrMo_{0.2} high-entropy alloy at high-velocity deformation, *J. Mater. Sci. Technol.* 139 (2023) 156–166.
- [44] A. Fu, B. Liu, Z. Li, B. Wang, Y. Cao, Y. Liu, Dynamic deformation behavior of a FeCrNi medium entropy alloy, *J. Mater. Sci. Technol.* 100 (2022) 120–128.
- [45] Z. Li, Z. Xia, S. He, F. Wang, X. Wu, Y. Zhang, L. Yan, F. Jiang, Dynamic mechanical properties of FGH4097 powder alloy and the applications of its constitutive model, *J. Mater. Res. Technol.* 22 (2023) 1165–1184.
- [46] H. Chen, W. Li, Y. Huang, Z. Xie, X. Zhu, B. Liu, B. Wang, Molten pool effect on mechanical properties in a selective laser melting 316L stainless steel at high-velocity deformation, *Mater. Charact.* 194 (2022) 112409.
- [47] R.A. Rowe, N. Holtham, P. Allison, A. Palazzotto, K. Davami, A comparison of high strain rate response and adiabatic shear band formation in additively and traditionally manufactured Inconel 718, *Mater. Charact.* 207 (2024) 113506.
- [48] E. Welsch, D. Ponge, S.M.H. Haghigat, S. Sandlöbes, P. Choi, M. Herbig, S. Zaeferrer, D. Raabe, Strain hardening by dynamic slip band refinement in a high-Mn lightweight steel, *Acta Mater.* 116 (2016) 188–199.
- [49] M.J. Yao, E. Welsch, D. Ponge, S.M.H. Haghigat, S. Sandlöbes, P. Choi, M. Herbig, I. Bleskov, T. Hickel, M. Lipinska-Chwalek, P. Shanthraj, C. Scheu, S. Zaeferrer, B. Gault, D. Raabe, Strengthening and strain hardening mechanisms in a precipitation-hardened high-Mn lightweight steel, *Acta Mater.* 140 (2017) 258–273.
- [50] F. Otto, A. Dlouhy, C. Somsen, H. Bei, G. Eggler, E.P. George, The influences of temperature and microstructure on the tensile properties of a CoCrFeMnNi high-entropy alloy, *Acta Mater.* 61 (2013) 5743–5755.
- [51] Y. Guo, M. Li, P. Li, C. Chen, Q. Zhan, Y. Chang, Y. Zhang, Microstructure and mechanical properties of oxide dispersion strengthened FeCoNi concentrated solid solution alloys, *J. Alloy. Compd.* 820 (2020) 153104.
- [52] Z. Li, Y. Gu, M.X. Pan, C.X. Wang, Z.Y. Wu, X.L. Hou, X.H. Tan, H. Xu, Tailoring AC magnetic properties of FeCoNi(MnSi)_x (0 ≤ x ≤ 0.4) high-entropy alloys by the addition of Mn and Si elements, *J. Alloy. Compd.* 792 (2019) 215–221.
- [53] H. Wen, T.D. Topping, D. Isheim, D.N. Seidman, E.J. Lavernia, Strengthening mechanisms in a high-strength bulk nanostructured Cu-Zn-Al alloy processed via cryomilling and spark plasma sintering, *Acta Mater.* 61 (2013) 2769–2782.
- [54] A.J. Ardell, Precipitation hardening, *Metall. Trans. A* 16 (1985) 2131–2165.
- [55] L. Yang, C. Wei, D. Liang, F. Jiang, Z. Cheng, J. Luan, Z. Jiao, F. Ren, Microstructure evolution and deformation mechanism of coherent L1₂-strengthened high-entropy alloy during sliding wear, *Compos. B Eng.* 256 (2023) 110651.
- [56] L. Fan, T. Yang, Y. Zhao, J. Luan, G. Zhou, H. Wang, Z. Jiao, C.T. Liu, Ultrahigh strength and ductility in newly developed materials with coherent nanolamellar architectures, *Nat. Commun.* 11 (2020) 6240.
- [57] Q. Xue, M.A. Meyers, V.F. Nesterenko, Self-organization of shear bands in titanium and Ti-6Al-4V alloy, *Acta Mater.* 50 (2002) 575–596.
- [58] M.A. Meyers, G. Subhash, B.K. Kad, L. Prasad, Evolution of microstructure and shear-band formation in α -hcp titanium, *Mech. Mater.* 17 (1994) 175–193.
- [59] U.S. Lindholm, G.R. Johnson, Material behavior under high stress and ultrahigh loading rates, in: J. Mescall, V. Weiss (Eds.), *Material Behavior under High Stress and Ultrahigh Loading Rates*, Springer US, Boston, 1983, pp. 61–79.
- [60] Z. Yang, M. Yang, Y. Ma, L. Zhou, W. Cheng, F. Yuan, X. Wu, Strain rate dependent shear localization and deformation mechanisms in the CrMnFeCoNi high-entropy alloy with various microstructures, *Mater. Sci. Eng. A* 793 (2020) 139854.
- [61] L.X. Liu, J. Pan, C. Zhang, J.Y. Xu, R. Guo, L. Liu, Achieving high strength and ductility in a 3D-printed high entropy alloy by cooperative planar slipping and stacking fault, *Mater. Sci. Eng. A* 843 (2022) 143106.
- [62] L.W. Meyer, S. Manwaring, *Metallurgical Applications of Shock-Wave and High-Strain-Rate Phenomena*, Marcel Dekker, New York, 1986.
- [63] Q. Xue, G.T. Gray, B.L. Henrie, S.A. Maloy, S.R. Chen, Influence of shock prestraining on the formation of shear localization in 304 stainless steel, *Metall. Mater. Trans. 36* (2005) 1471–1486.
- [64] Q. Xue, G.T. Gray, Development of adiabatic shear bands in annealed 316L stainless steel: Part I. Correlation between evolving microstructure and mechanical behavior, *Metall. Mater. Trans. A* 37 (2006) 2435–2446.
- [65] J.X. Xing, F.P. Yuan, X.L. Wu, Enhanced quasi-static and dynamic shear properties by heterogeneous gradient and lamella structures in 301 stainless steels, *Mater. Sci. Eng. A* 680 (2017) 305–316.
- [66] V.A. Pushkov, A.V. Yurlov, A.M. Podurets, A. Kal'manov, E. Koshatova, Superior dynamic shear properties by structures with dual gradients in medium entropy alloys, *EPJ Web Conf.* 10 (2010) 00029.

- [67] F.P. Yuan, X.D. Bian, P. Jiang, M.X. Yang, X.L. Wu, Dynamic shear response and evolution mechanisms of adiabatic shear band in an ultrafine-grained austenite-ferrite duplex steel, *Mech. Mater.* 89 (2015) 47–58.
- [68] V.A. Pushkov, A.V. Yurlov, A.M. Podurets, A.N. Tsibikov, M.I. Tkachenko, A.N. Balandina, Effect of preloading on the formation of adiabatic localized shear in copper, *Combust. Explos. Shock Waves* 49 (2013) 620–624.
- [69] U. Hofmann, E. El-Magd, Behaviour of Cu-Zn alloys in high speed shear tests and in chip formation processes, *Mater. Sci. Eng. A* 395 (2005) 129–140.
- [70] Y.B. Gu, V.F. Nesterenko, Dynamic behavior of HIPed Ti-6Al-4V, *Int. J. Impact Eng.* 34 (2007) 771–783.
- [71] J.Y. Zhang, Z.K. Zhao, Q. Li, J.H. Luan, C.T. Liu, Y.L. Zhao, T. Yang, Understanding the impacts of Li_2 nanoprecipitates on the electrochemical and passive behavior of CoCrNiAlTi-type high-entropy alloys, *Adv. Powder Mater.* 2 (2023) 100113.
- [72] K. Jiang, Q. Zhang, J. Li, X. Li, F. Zhao, B. Hou, T. Suo, Abnormal hardening and amorphization in an FCC high entropy alloy under extreme uniaxial tension, *Int. J. Plast.* 159 (2022) 103463.
- [73] Y.H. Jo, D.G. Kim, M.C. Jo, K.Y. Doh, S.S. Sohn, D. Lee, H.S. Kim, B.J. Lee, S. Lee, Effects of deformation-induced BCC martensitic transformation and twinning on impact toughness and dynamic tensile response in metastable VCrFeCoNi high-entropy alloy, *J. Alloys Compd.* 785 (2019) 1056–1067.
- [74] H. Liu, C. Kuo, P. Shen, C. Huang, H. Yen, C. Tsai, Disordering of Li_2 phase in high-entropy alloy deformed at cryogenic temperature, *Adv. Eng. Mater.* 23 (2021) 2100564.
- [75] A.P. Thompson, H.M. Aktulga, R. Berger, D.S. Bolintineanu, W.M. Brown, P.S. Crozier, P.J. in't Veld, A. Kohlmeyer, S.G. Moore, T.D. Nguyen, R. Shan, LAMMPS—a flexible simulation tool for particle-based materials modeling at the atomic, meso, and continuum scales, *Comput. Phys. Commun.* 271 (2022) 108171.
- [76] D. Farkas, A. Caro, Model interatomic potentials for Fe-Ni-Cr-Co-Al high-entropy alloys, *J. Mater. Res.* 35 (2020) 3031–3040.
- [77] A. Stukowski, Visualization and analysis of atomistic simulation data with OVITO—the open visualization tool, *Model. Simulat. Mater. Sci. Eng.* 18 (2010) 015012.
- [78] M. Parrinello, A. Rahman, Polymorphic transitions in single crystals: a new molecular dynamics method, *J. Appl. Phys.* 52 (1981) 7182–7190.
- [79] W. Andreoni, S. Yip, *Handbook of Materials Modeling: Methods: Theory and Modeling*, second ed., Springer, Berlin, 2020.
- [80] W.Z. Polak, Efficiency in identification of internal structure in simulated monoatomic clusters: comparison between common neighbor analysis and coordination polyhedron method, *Comput. Mater. Sci.* 201 (2022) 110882.



Ao Fu is a Lecturer in the Powder Metallurgy Research Institute at Central South University. He achieved his PhD degree from the Central South University in 2021 and subsequently worked as a Postdoctoral Fellow in the Powder Metallurgy Research Institute at the Central South University. His research interest focuses on the fabrication and mechanical behavior of advanced powder-metallurgy materials.



Bin Liu is a Vice Dean of the Powder Metallurgy Research Institute at the Central South University. He received his PhD degree in 2008 from the Central South University. His current research interests focus on the preparation, deformation, and strengthening behaviors of advanced powder-metallurgy materials.



Marc André Meyers is a Distinguished Professor of Materials Science at the University of California San Diego. His research field is the mechanical behavior of materials with a focus on three areas: dynamic behavior of materials, nanocrystalline materials, and biological materials. His honors include Fellow, TMS, APS, ASM, Explorers Club, and member of the Brazilian and Luxembourg Academies of Sciences. He was a cofounder of the Center for Explosives Technology Research, New Mexico Tech, and the EXPLOMET conference series, as well as Associate Director and Director of the UCSD Institute for Mechanics and Materials.



Yong Liu is the Dean of the Powder Metallurgy Research Institute at the Central South University and member of Alexander von Humboldt fellowship for experienced researchers. He received his PhD degree from Central South University in 1999, and worked as a Postdoctoral Fellow at the Oak Ridge National Laboratory and the University of Tennessee from 2005 to 2006. His current research interests mainly focus on the advanced powder-metallurgy metallic materials and ceramics.